Journal of Materials Chemistry C

Accepted Manuscript

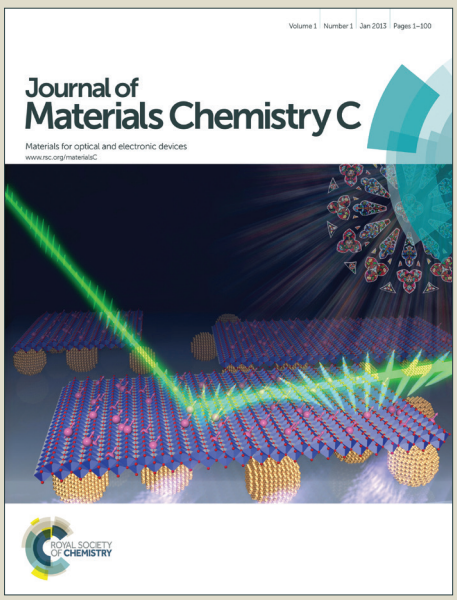

ROYAL SOCIETY OF CHEMISTRY

www.rsc.org/materialsC

Raman Scattering and Photoluminescence Investigation of $YBO_3:Eu^{3+}$ under High Temperature and High Pressure

W.S. Song[a], G.X.Y. Huang[a], R.C. Dai[b*], Z.P.Wang[b] and Z.M. Zhang[b*]

[a]*School of the Gifted Young, University of Science and Technology of China, Hefei, Anhui 230026, China;*

[b]*The Centre of Physical Experiments, University of Science and Technology of China, Hefei, Anhui 230026, China*

*Corresponding authors: zzm@ustc.edu.cn, dairc@ustc.edu.cn

Raman scattering, X-ray diffraction and Photoluminescence spectra of $YBO_3:Eu^{3+}$ are measured at high temperatures up to 1323 K. Results show that a temperature-induced phase transition from the LT to HT phase starts at about 1273 K, then the HT phase transforms into LT phase as cooling to 873 K. A theoretical model based on luminescent dynamic process describes the temperature-dependent emission intensity well. In this model, the contributions from thermal activation, phonon-assisted absorption, and nonradiative energy transfer are analyzed in details. Additionally, we report the structure and optical behavior of $YBO_3:Eu^{3+}$ under high pressure by means of Raman scattering and photoluminescence measurements. When pressure is increased from zero to 25 GPa, Raman and Photoluminescence shown that the structure of $YBO_3:Eu^{3+}$ keeps stable, and no pressure-driven phase transition occurs in the entire pressure range in these experiments. Also the mode-Grüneisen parameters and thermal expansion coefficient are calculated.

Introduction

$YBO_3:Eu^{3+}$ is widely applied in plasma display panels, Hg-free fluorescent lamps and light-emitting diodes for its high vacuum ultraviolet transparency, excellent high luminescence efficiency, strong chemical and structure stability[1-5]. Up to now, as far as quantum efficiency and vacuum ultraviolet absorption, $YBO_3:Eu^{3+}$ is still one of the best red phosphors. However, the characteristic emission of $^5D_0 \rightarrow {}^7F_1$ is almost equal to the transition $^5D_0 \rightarrow {}^7F_2$, which gives rise to an orange-red emission and relatively poor color chromaticity. Nevertheless, the $^5D_0 \rightarrow {}^7F_2$ transition is hypersensitive to the symmetry of local crystal field surrounding Eu^{3+} ions and that transition would be relatively strong if the crystal field symmetry is low Therefore, several researchers attempt to solve the chromaticity drawback of $YBO_3:Eu^{3+}$ by the means of reducing the symmetry of the crystal field.

Many investigators devote to enhancing the $^5D_0 \rightarrow {}^7F_2$ emission through various chemical means, such as controlling the morphology and size of $YBO_3:Eu^{3+}$. Wei *et al* synthesized sphere-like $YBO_3:Eu^{3+}$ nanoparticles and found that red and orange (R/O) intensity ratio is much higher in the smaller sized particles[4]. They thought that distorted crystal lattices should be responsible for the superior chromaticity. Zhang *et al* reported the hierarchical architecture of $YBO_3:Eu^{3+}$ with nano- and micro-structure and considered that the improvement in color chromaticity was attributed to distinct multilayer of the samples[6]. Besides, the luminescence intensity of $YBO_3:Eu^{3+}$ can be also enhanced by co-dopant Bi^{3+}, Li^+ and alkaline-earth metal ions[7, 8], which play important roles in tunning energy transfer process, particle size and surface morphology.

A well-defined crystal structure of the compounds is crucial to improve the fluorescence performance and luminescence properties. YBO_3 exists in two types of phase structures: low-temperature (LT) phase and high-temperature (HT) phase. The LT phase is a monoclinic cell with *C*2/c space group, in which B_3O_9 rings are the only borate species under ambient condition, while the HT phase crystallizes in a monoclinic cell with all isolated plane BO_3 groups under the *C*2/c space symmetry[9]. Gu et al. investigated the structure of YBO_3 with temperatures using *in situ* Raman spectroscopy, and observed a reversible structural transition from LT phase to HT phase[10]. High-pressure X-ray diffraction study of YBO_3/Eu^{3+} was performed by Wang et al. and they found $YBO_3:Eu^{3+}$ stabilizes up to 41 GPa[11]; the bulk moduli of $YBO_3:Eu^{3+}$ was refined to be 141 GPa by Errandonea et al[12].

Despite the advances mentioned above, the present understanding about the structure and optical properties of $YBO_3:Eu^{3+}$ is not sufficient, especially for high temperature and high pressure. It is well known that Eu^{3+} ions are sensitive to local environment, thus presence and splitting of the selected Eu^{3+} electronic transitions could be an excellent probe to structural studies. In this article, the temperature- and pressure-dependent structure and optical behavior of $YBO_3:Eu^{3+}$ are investigated in detail using Raman scattering method and Eu^{3+} luminescence probe technique.

Experimental

Sample preparation

$YBO_3:Eu^{3+}$ is prepared by solid-state reaction. 4.5 mmol Y_2O_3 (99.99% purity), 0.5 mmol Eu_2O_3 (99.99% purity) and 10.25 mmol H_3BO_3 (99.99% purity) are mixed (H_3BO_3 is 2.5 mol % excess

on account of the volatility of B_2O_3). At first, the mixture is ground for 1h and then heated at 500 °C for 2h to decompose the boric acid. After cooling down to room temperature the mixture are ground for 1 h and heats again at 1100 °C for 2 h.

Characterization

X-ray diffraction (XRD) was carried out on X-ray diffractometer (Rigaku, TTR Ⅲ) under Cu Kα radiation. The size and morphology were characterized by a field emission scanning electron microscope (FE-SEM, SU8010). Emission and excitation spectra were collected by a steady-state/lifetime spectrofluorimeter (JOBIN YVON, FLUOROLOG-3-TAU) equipped with a 450 W xenon lamp as excitation source. PL and Raman spectra are collected by an integrated laser Raman system (LABRAMHR, Jobin Yvon) with a confocal microscope, a stigmatic spectrometer, and a multichannel air cooled charge coupled device (CCD) detector. High temperature measurements were carried out in flowing high pure nitrogen in a TS 1500 furnace (Linkam, England). The sample was heated to the desired temperature with 50 K increments per step and held for 10 min before collecting Raman spectra under ambient pressure. We use 514.5 nm excitation at 1323 K and 785 nm excitation at other temperatures to prevent the effects of fluorescence to the largest extent. High pressure was generated by using diamond anvil cell (DAC) technique with a stainless steel gasket. The 200 μm gasket was preindented and then a hole in a diameter of 170 μm was made in its center by a spark driller. Silicon oil was used as pressure transmitting medium. A few grains of ruby powder were applied for in situ measurements of pressure by using the standard ruby fluorescence technique[13]. The pressure was calibrated by the shift of the ruby R_1 fluorescence line.

Results and discussion

Characterization of $YBO_3:Eu^{3+}$

Fig. 1 shows SEM images of fresh $YBO_3:Eu^{3+}$ sample and after 1573 K annealing sample. The as-synthesized sample is agglomeration of small particles with diameters from 100 nm to 500 nm. After annealing at 1573 K, The particles grow and coagulate and the boundaries between particles become hard to identify. Fig. 2 displays the XRD pattern of $YBO_3:Eu^{3+}$ sample at room temperature. All the diffraction peaks of these samples can be matched well with ICDD Card No. 04-014-2922, and the crystal structure are indexed to a pure LT phase YBO_3, crystallizing in a monoclinic pseudowollastonite-type structure with *C*2/c space group [9, 14, 15]. No additional peak of other phase has been found, which also indicates that the existence of Eu^{3+} does not cause significant change in the host structure and the obtained samples are single phase.

The excitation spectra of $YBO_3:Eu^{3+}$ with emission wavelengths 621.5nm and 610.5 nm are given in Fig. 3 at ambient condition, separately. The intense edge from 250 nm to 270 nm corresponds to the charge transfer (CT) between O^{2-} and Eu^{3+}. The characteristic absorption peaks of Eu^{3+} ions corresponding to the direct excitation from the ground state to higher excited states of europium f-electrons can be observed in the range of 280-550 nm (assigned in Fig.3)[7]. The upper right inset of Fig. 3 is phonon side band (PSB), in which zero phonon line is at 465 nm and one phonon line is around 445 nm for $^7F_0 \rightarrow {}^5D_2$ transition. Therefore, the Huang-Rhys factor (*S*) can be calculated as follows[16]:

$$S = I_{1p} / I_{zp} \quad (1)$$

Where I_{1p} and I_{zp} are intensities of one phonon line and zero phonon line, separately. The S value is 0.080. This factor is an important constant for constructing luminescent dynamic equation.

The emission spectra of $YBO_3:Eu^{3+}$ at ambient condition with 514.5 nm excitation are shown in Fig. 4. Normally, Eu^{3+} generates luminescence due to the transitions from excited $^5D_0$ level to ^7F_J $(J = 0, 1, 2, 3, 4)$ levels of the $4f^6$ configuration. The Eu^{3+} characteristic emissions peaks around 581 nm are from $^5D_0 \rightarrow {}^7F_0$ transition; the peaks in the range of 585-595 nm originate from $^5D_0 \rightarrow {}^7F_1$ transition; the lines from 600 to 640 nm range are assigned to $^5D_0 \rightarrow {}^7F_2$ transition; several peaks in the range of 640-660 nm are due to $^5D_0 \rightarrow {}^7F_3$ transition. The number of splits is closely interrelated with specific local sites occupied by the Eu^{3+} ions. As for $YBO_3:Eu^{3+}$ with $C2/c$ space group, Eu^{3+} ion mainly occupies in C_1 and C_i sites of Y^{3+} ion[17]. For C_1, numbers of bands for each $^5D_0 \rightarrow {}^7F_J$ $(J = 0, 1, 2, 3, 4)$ transition are 1, 3, 5, 7 and 9, separately; for C_i, the numbers correspond to 0, 3, 0, 0 and 0. So the number of bands in PL spectra should be 1 for $^5D_0 \rightarrow {}^7F_0$, 6 for $^5D_0 \rightarrow {}^7F_1$, 5 for $^5D_0 \rightarrow {}^7F_2$, and 7 for $^5D_0 \rightarrow {}^7F_3$ (other splits are not taken into consideration). The emission spectra can be decomposed to several Lorentz lineshape peaks, which are all in accordance with theoretical splitting number as seen in Fig. 4. This consistence confirms the sites symmetry of Y^{3+} and space group of $YBO_3:Eu^{3+}$. Combining with excitation spectra, values of energy levels of Eu^{3+} are listed in Table 1.

Raman spectrum of $YBO_3:Eu^{3+}$ at ambient condition is shown in the bottom of Fig. 5. LT phase $YBO_3:Eu^{3+}$ exhibits typical vibrational bands of B_3O_9 rings. The B_3O_9 ring has D_{3h} symmetry with twelve atoms, which leads to 20 vibrational modes represented as[10]:

$$\Gamma = 4A_1' + A_1'' + 2A_2' + 3A_2'' + 6E' + 4E''$$

Among which $4A_1' + 6E' + 4E''$ are Raman active. The B–O–B bending of BO_4 units includes Raman bands at 260 cm^{-1}, 295 cm^{-1}, 358 cm^{-1}, 378cm^{-1}, 413 cm^{-1}, 432 cm^{-1}, 490 cm^{-1} and 508 cm^{-1}, and B_3O_9 borate ring deformation includes Raman bands at 614 cm^{-1}, 669 cm^{-1}, 723 cm^{-1} and 837 cm^{-1}, while the 1003 cm^{-1} and 1035 cm^{-1} bands can be assigned to stretching of tetrahedral BO_4 groups, which share vertices, thus forming three-member ring borate B_3O_9 units. And Raman modes under 250 cm^{-1}, such as 166 cm^{-1}, 189 cm^{-1} and 205 cm^{-1} are contributed to the translation of the Y^{3+} cations and the B_3O_9 groups[18]. All these Raman peaks provide evidences of existence of B_3O_9 rings in LT phase.

Temperature-dependent Raman, XRD and PL spectra

Fig. 5 shows the Raman spectra of $YBO_3:Eu^{3+}$ at different temperatures under ambient pressure. With increasing temperature, Raman peaks shift to low-frequency and the corresponding intensities decrease. These are due to temperature-induced interatomic distances increasing and bond angle distribution widening, causing distortions of the crystal structure[19]. When the temperature reaches 1323 K, some new Raman peaks appear obviously, corresponding to isolated BO_3 triangles. The point group symmetry of the isolated BO_3 group is D_{3h}, which leads to vibrational modes represented as[10]: $\Gamma = A_1' + A_2'' + 2E''$. Characteristic Raman peaks of BO_3 units were observed at around 940 cm^{-1}, assigned to the symmetric stretching mode $A_1'(\upsilon_1)$, which splits into two Raman peaks since the occupation site of the BO_3 group is less than threefold symmetry in the HT phase; and at around 1200 cm^{-1}, assigned to the asymmetric stretching mode $E'(\upsilon_3)$. Besides, the Raman bands between 620 cm^{-1} and 800 cm^{-1} are assigned to out-plane

bending mode $A_2''(\upsilon_2)$. These bands prove the existence of BO_3 group in the HT phase YBO_3[10]. Moreover, vibrational modes at 159 cm^{-1}, 226 cm^{-1} ,331 cm^{-1} could be the translation of the Y^{3+} cations and the BO_3 units. It can be concluded that during the heating process, the B–O bonds of the BO_4 groups break apart and isolated BO_3 plane conjugated groups are formed. As presented in ESI Fig. S1a, temperature-dependent XRD confirms that LT phase transformation into HT phase in YBO_3:Eu^{3+} starts at 1273 K. During cooling process, Raman spectra reveal the HT phase of YBO_3:Eu^{3+} transforms into LT phase at 863 K, which is consistent with observation in XRD pattern of YBO_3:Eu^{3+} as shown in ESI Fig. S1b. There is a large thermal hysteresis existing between these two phase transitions. The reason is that the phase transformation of YBO_3 has higher apparent activation energy for heating process, forming a large potential barrier[20].

Fig. 6 is the PL emission spectra of YBO_3:Eu^{3+} from 294 to 1323 K under 514.5 nm excitation. With increasing temperature, the $^5D_0 \rightarrow {}^7F_0$ transition only has one emission band, and the emission peak linearly shifts toward shorter wavelength. For the $^5D_0 \rightarrow {}^7F_1$ transition, at 294 K, six obvious peaks can be distinguished in the region of 590-595 nm (also seen in Fig. 4); when the temperature reaches 523 K, two new peaks appear at 583 and 585 nm, of similar location with PL spectra of Eu^{3+} in Y_3BO_6[21]. As discussed above, the two site occupations C_i and C_1 in YBO_3:Eu^{3+} can only lead to a single peak for $^5D_0 \rightarrow {}^7F_0$. Y_3BO_6 has various kinds of symmetry sites which would bring about complicated splitting of energy levels, especially distinct multi-peaks for $^5D_0 \rightarrow {}^7F_0$, as described in reference [17]. However, since only one peak can be observed for $^5D_0 \rightarrow {}^7F_0$, and the XRD pattern also indicates pure phase for YBO_3, there is no sign of Y_3BO_6 phase existence. It can be deduced that 10 mol % doping of Eu^{3+} possibly brings in some new local symmetry similar to that in Y_3BO_6, without changing phase purity. The new splits of

$^5D_0 \rightarrow {}^7F_1$ transition caused by this doping effect are too weak to detect at room temperature, but when the temperature increases, these new peaks become stronger. The six peaks merge into three peaks in the 590-595 nm and two new peaks are kept for the $^5D_0 \rightarrow {}^7F_1$ transition from 623 to 1323 K. As to the $^5D_0 \rightarrow {}^7F_2$ transition, it has three emission peaks located in a range of 605-615 nm, and two peaks in 620-635 nm at 294 K. With the increase of temperature, the former three emission peaks gradually merge into one peak and the latter two peaks also broaden into one peak. The results show that the position of the $^5D_0 \rightarrow {}^7F_2$ transition hardly move with the increasing temperature. As to the $^5D_0 \rightarrow {}^7F_3$ transition, peaks do not shift butbecome wider with the increasing temperature. The phase transition in heating process can hardly be detected from the PL spectra, due to the emissions of $YBO_3:Eu^{3+}$ HT phase are undistinguishable in strong thermal radiation background at 1373 K. As presented ESI Fig. S2, the R/O value increases monotonically with increasing temperature, indicating temperature can effectively improve color chromaticity in the $YBO_3:Eu^{3+}$. During cooling process, PL spectra gradually become distinguishable at the temperature of 1173 K. New emission peaks at 578, 587 and 617 nm appear while original peaks disappear, indicating a big change of local sites symmetry. This is a sign of phase transition and characteristic emissions of HT-phase $YBO_3:Eu^{3+}$ are clearly observed. When the temperature decreases to 873 K, the PL spectra gradually become similar to that of the starting materials, indicating the HT phase transforms into LT-phase. In the cooling process, an abrupt leap in R/O is found at 873 K as shown in ESI Fig. S2, suggesting the HT phase transforms into LT phase at this temperature.

The decay curves for the $YBO_3:Eu^{3+}$ monitored at 593 nm for Eu^{3+} emission are measured from 298 K to 673 K and are displayed in Fig. 7. All the decay curves can be well fitted via

single-exponential function. It is obvious that increasing temperature from 298 K to 673 K leads to slightly shortening the Eu^{3+} lifetime (that is, from 3.16 ms to 2.81 ms). In this case, energy transfer between Eu ions and non-radiative decay at defects are more likely to take place, thus resulting in a shorter lifetime.

Fig. 8 shows temperature-dependent total emission intensity of the $^5D_0 \rightarrow {}^7F_J \quad (J = 0, 1, 2, 3)$ transitions under 514.5 nm excitation. With increasing temperature, the intensity presents a maximum at about 900 K. The process can be explicated by a model base on luminescence dynamic equation, considering thermal activation, phonon-assisted absorption, and nonradiative energy transfer process[22]. For $YBO_3:Eu^{3+}$, whose splitting energy levels have already been determined previously, the total emission intensity of $\sum_J {}^5D_0 \rightarrow {}^7F_J (J = 0, 1, 2, 3)$ can be written as:

$$I(T) \propto \frac{\sum IN_i(T)\sigma_i(T)}{1 + W_T(T) / \gamma_0} \tag{2}$$

Where I is the pumping light power density, W_T is temperature-quenching rate, γ_0 is radiative transition rate and $\sigma_i(T)$ is absorption cross section. $N_i(T) = \frac{e^{-\Delta E_i / kT}}{\sum_i e^{-\Delta E_i / kT}}$ is thermal electron population on different splitting levels in ^7F_J, i represents each splitting energy level and ΔE_i is energy separation from these levels to $^7F_0$. k is the Boltzmann Constant. Moreover, multi-phonon absorption, resonant absorbing process, and temperature-quenching rate are taken into account, and the fitting formula can be written as

$$I(T)=\frac{\beta_1[\sum_{i,j} e^{-\alpha E_{i,j}} \times (1+\langle n\rangle)^{E_{ij}/h\omega} + \sum_{i,k} e^{-\alpha E_{ik}} \times \langle n\rangle^{E_{ik}/h\omega}]e^{-\Delta E_i/kT}}{\sum_i e^{-\Delta E_i/kT} \times (1+\beta_3 e^{T/T_c})} + \frac{\beta_2 e^{-\Delta E_i/kT}}{\sum_i e^{-\Delta E_i/kT} \times (1+\beta_3 e^{T/T_c})} \quad (3)$$

in which $\beta_1 = I\sigma_1, \beta_2 = I\sigma_2$, and $\beta_3 = W_T(0)/\gamma_0$. The right side of Eq. (3) includes two terms. The former mainly illustrates multi-phonon absorption processes. For non-resonant excitation, the electrons can reach $^5D_{0,1,2}$ levels with the assistant of phonons (higher ^5D_J states are not taken into consideration since the transition probability is too small to accumulate enough electrons). On the denominator, the sum term including subscript *i, j* and *i, k*, presents absorbing and emitting phonon process, respectively. $E_{i,j}$ and $E_{i,k}$ are energy differences between the energy of a 514.5 nm photon and the energy separation from the target transition levels. In the first term, $\alpha = \frac{1}{h\omega}\left[In(E_{i,j(k)}/h\omega) - 1 - Ins\right]$, where s is Huang–Rhys factor, providing a quantitative description of electron-phonon coupling. $n = \frac{1}{e^{h\omega/kT}-1}$ is the phonon density. As to the second term, resonant absorption process is demonstrated. In consideration of the $^7F_3$ splitting stark levels, the 514.5 nm excitation can be in resonance with $^7F_3 \rightarrow {}^5D_2$ transition. Note that other possible transitions from the higher ^7F_J states are neglected due to the very low thermal electron populations compared to the $^7F_{1,2,3}$. Besides, the $\frac{1}{1+\beta_3 e^{T/T_c}}$ item coexisting in two terms is arisen from temperature-quenching effect. Energy levels of Eu^{3+} in YBO_3:Eu^{3+} are given in Table 1. Other constants are listed as below: Huang-Rhys factor s=0.080, calculated from Phonon side band (PSB) spectra; Boltzmann Constant k = 0.6948 cm^{-1}/K; $h\omega$ =1035 cm^{-1}, obtained from Raman spectra.

As seen in Fig. 8, the emission intensity with temperature can be well fitted and fitting parameters are determined as, β_1 =0.22, β_2 =164.19, β_3 =5.05×10^{-8}, T_c =58.11. The contribution of

multi-phonon assisted absorption and resonant absorption processes are displayed respectively. The emission intensity derived from the multi-phonon assisted absorption process, exhibits overall declining trend with increasing temperature; while the resonant absorption process, which plays a dominant role in luminescence, has a maximum emission intensity around 900 K. Thus, the emission intensity with temperature can be ascribed to two main factors. The upper left insert of Fig. 8 gives the thermal electron population with temperatures. The population number $^7F_3$ level increases with temperature. This indicates that the first dominating factor is the excitation from $^7F_3$ to $^5D_2$, which can make the emission intensity increase monotonically in temperature range of 294-1323 K. The second one is the temperature-quenching effect, causing the emission intensity decreases with temperature. The theoretical model and fitting results help to improve our understanding of luminescence dynamic process of $YBO_3:Eu^{3+}$.

Pressure-dependent PL and Raman spectra

Fig. 9 shows the PL emission spectra of $YBO_3:Eu^{3+}$ under high pressure up to 25 GPa. With the increasing of pressure, the $^5D_0 \rightarrow {}^7F_{0,1}$ transitions almost shift linearly to longer wavelength and broaden, meanwhile their emission intensities decrease. The red-shift is due to the fact that the pressure strengthens the interaction between Eu^{3+} and O^{2-} ions, thus energy levels of $^5D_0$ and $^7F_{0,1}$ will get close and the energy level difference decreases. For $^5D_0 \rightarrow {}^7F_2$ transition, the four obvious peaks between 605 and 620 nm gradually merge into one and the right peak slightly blue-shifts with pressure. For the band from 625 to 630 nm, there is an obvious red-shift with a comparatively high rate. With pressure increasing, a left peak gradually diminishes while a new peak in the right appears slowly around 14.7 GPa. This could be caused by pressure-induced

change of site symmetry. The reason why two groups of $^5D_0 \rightarrow {}^7F_2$ peaks move to opposite directions is that the electric dipole driving $^5D_0 \rightarrow {}^7F_2$ transition from 608 to 634 nm is easily affected by crystal field. The increase of pressure results in smaller distances and stronger interaction between atoms, thus strengthening crystal field around Eu^{3+}. This aggravates the splitting of $^7F_2$, and the two groups of peaks gradually separate, causing the blue-shift of high-energy peaks and red-shift of low-energy peaks. Moreover, the ratio of R/O decreases with the increase of pressure as seen in ESI Fig. S3, indicating that the site symmetry rises and the covalency of Eu–O bond weakens. Since no apparent discontinuity can be observed in ESI Fig. S3, we can deduce that no phase transitions happened in the increasing of pressure. When the pressure is released, the PL spectrum recovers to the original state, suggesting a good stability of YBO_3:Eu^{3+} under high pressure up to 25 GPa.

Figure 10 displays the evolution of Raman modes of YBO_3:Eu^{3+} with increasing pressure. This exhibits a shift to high frequency and broadening of Raman peaks without change of line shape. The intensities of these peaks diminish quickly with pressure and most peaks cannot be identified above 10 GPa due to the pressure-induced broaden effect. Still, several characteristic modes of B_3O_9 can be identified and the frequencies of them increase to high wavenumber at different rates. The reason is that the pressure reduces the distances between atoms, leading to the increase of vibration energy. From the Raman spectra, several physical interesting parameters can be obtained, including pressure coefficients, which reflect Raman modes shifting rates; and Grüneisen parameter γ, which plays a crucial role in understanding the thermodynamic and thermoelastic behavior of solids; as well as molar heat capacity and thermal expansion coefficient[23]. Through

linear fitting, pressure coefficients $d\omega / dP$ are calculated from Raman spectra. Mode Grüneisen parameter γ_i can be calculated by [24, 25]

$$\gamma_i = -\left(\frac{\partial In\ \omega_i}{\partial In\ V}\right) = \frac{B}{\omega_{0i}}\left(\frac{d\omega_i}{dP}\right) \quad (4)$$

In which ω_{0i} is the frequency of the vibrational mode and B is the bulk modulus whose value is 141 GPa [12]. The molar heat capacity of a single mode can be expressed as[23],

$$C_i = R\frac{(E_i / k_B T)^2 e^{E_i/k_B T}}{(e^{E_i/k_B T} - 1)^2} \quad (5)$$

where $E_i = h\nu_i$ is the energy of single vibrational mode, while k_B is Bolztmann constant. R is the ideal gas constant. The values of Raman modes at ambient pressure ω_i, pressure coefficient $d\omega_i /dp$, mode Grüneisen parameter γ_i and single mode molar heat capacity C_i are listed in table 2. With that, we can calculate the total heat capacity at constant volume $C_v = \sum C_i = 61.44$ and average Grüneisen parameter $\gamma_{av} = \sum C_i \gamma_i / C_v = 0.87$. Since the γ_{av} can be also expressed as $\gamma_{av} = 3\alpha V_m B_0 / C_v$, and molar unit-cell volume at ambient pressure V_m is 6.56×10^{-5} $m^3 \cdot mol^{-111}$, we can obtain the linear thermal expansion coefficient α as 1.93×10^{-6} K^{-1}. Since Grüneisen parameter γ and thermal expansion coefficient α of $YBO_3:Eu^{3+}$ are not reported so far, the values of γ and α in our calculation gives a necessary understanding of $YBO_3:Eu^{3+}$ thermoelastic behavior. On the release of pressure, Raman peaks gradually recover to starting state, indicating the structure of $YBO_3:Eu^{3+}$ is fairly stable up to 25 GPa.

Conclusions

At ambient pressure, Raman scattering and XRD show that a reversible phase transition from LT phase to HT phase takes place at about 1273 K. From the PL spectra, the local sites of Eu^{3+} in YBO_3 crystal are well interpreted to be C_1 and C_i based on the splitting of $^5D_0 \rightarrow {}^7F_{0,1,2,3}$ transitions. This corroborates the *C*2/*c* space group of YBO_3, in accordance with the neutron diffraction study of Lin et al[9]. After heating-induced phase transition, the characteristic emissions of HT-phase YBO_3:Eu^{3+} are clearly observed as temperature cooling to 1173 K, and then turn into that of LT-phase at 873 K. This observation of phase transition is consistent with the results by Raman scattering and XRD. The R/O ratio of Eu^{3+} ion increases with temperature increasing, and an abrupt leap in R/O ratio is found with decreasing temperature to 873 K. Besides, the temperature-dependent emission intensity can be well calculated by a theoretical model based on the luminescence dynamic equations. As for ambient temperature, Raman scattering reveals that the structure of YBO_3:Eu^{3+} keeps stable at pressure of 25 GPa. The Grüneisen parameters γ and thermal expansion coefficient α of YBO_3:Eu^{3+} are 0.87 and 1.93×10^{-6} K^{-1}. The emissions of YBO_3:Eu^{3+} shift to long wavelength and R/O ratio reduces with the increase of pressure indicates lowering asymmetry around Eu^{3+} ions while no phase transition takes place on compression. Therefore, the luminescence of Eu^{3+} ion can serve as an excellent probe to structural studies of material.

Acknowledgements

This work was supported by the National Natural Science Foundation of China (No. 11304300), the National Basic Research Program of China (Nos. 2011CB932801 and 2012CB933702), the

Fundamental Research Funds for the Central Universities (Grant No. WK2030420002) and Anhui Provincial Natural Science Foundation (1308085QA06)

Notes and references

1. W. Chen and A. Zhou, *J. Phys. Chem. C*, 2012, 116, 24748-24751.
2. V. Jubera, J. P. Chaminade, A. Garcia, F. Guillen and C. Fouassier, *J. Lumin.*, 2003, 101, 1-10.
3. Z. Li, J. Zeng and Y. Li, *Small*, 2007, 3, 438-443.
4. Z. Wei, L. Sun, C. Liao, J. Yin, X. Jiang, C. Yan and S. Lü, *J. Phys. Chem. B*, 2002, 106, 10610-10617.
5. X.-C. Jiang, C.-H. Yan, L.-D. Sun, Z.-G. Wei and C.-S. Liao, *J. Solid State Chem.*, 2003, 175, 245-251.
6. X. Zhang, A. Marathe, S. Sohal, M. Holtz, M. Davis, L. J. Hope-Weeks and J. Chaudhuri, *J. Mater. Chem.*, 2012, 22, 6485-6490.
7. L. Chen, G. Yang, J. Liu, X. Shu, G. Zhang and Y. Jiang, *J. Appl. Phys.*, 2009, 105, 013513.
8. D. Jin, J. Yang, X. Miao, L. Wang, S. Guo, N. Wang and L. Wang, *Mater. Lett.*, 2012, 79, 225-228.
9. J. Lin, D. Sheptyakov, Y. Wang and P. Allenspach, *Chem. Mater.*, 2004, 16, 2418-2424.
10. G. X. Gu, D. Wang, X. S. Lv, S. M. Wan, J. L. You, Q. L. Zhang and S. T. Yin, *Mater. Chem. Phys.*, 2011, 131, 274-277.
11. P. Wang, D. He, C. Xu, X. Ren, L. Lei, S. Wang, F. Peng, X. Yan, D. Liu, Q. Wang, L. Xiong and J. Liu, *J. Appl. Phys.*, 2014, 115, 043507.
12. D. Errandonea, A. Muñoz and J. Gonzalez-Platas, *J. Appl. Phys.*, 2014, 115, 216101.
13. **H. K. Mao, P. M. Bell, J. W. Shaner and D. J. Steinberg, *J. Appl. Phys.*, 1978, 49, 3276-3283**.
14. P. Morgan, P. Carroll and F. Lange, *Mater. Res. Bull.*, 1977, 12, 251-259.
15. A. Pitscheider, R. Kaindl, O. Oeckler and H. Huppertz, *J. Solid State Chem.*, 2011, 184, 149-153.
16. Y. Tian, X. Qi, X. Wu, R. Hua and B. Chen, *J. Phys. Chem. C*, 2009, 113, 10767-10772.
17. G. Jia, P. A. Tanner, C.-K. Duan and J. Dexpert-Ghys, *J. Phys. Chem. C*, 2010, 114, 2769-2775.
18. Y. Wu, D. Ding, F. Yang, S. Pan and G. Ren, *Mater. Res. Bull.*, 2012, 47, 106-110.
19. G. E. Walrafen, S. R. Samanta and P. N. Krishnan, *J. Chem. Phys.*, 1980, 72, 113-120.
20. J. Plewa and T. Jüstel, *J. Therm. Anal. Calorim.*, 2007, 88, 531-535.
21. D. Boyer, G. Bertrand-Chadeyron, R. Mahiou, A. Brioude and J. Mugnier, *Opt. Mater.*, 2003, 24, 35-41.
22. J. Wang, H. Song, X. Kong, W. Xu and H. Xia, *J. Appl. Phys.*, 2002, 91, 9466-9470.

23. J. Ruiz-Fuertes, D. Errandonea, O. Gomis, A. Friedrich and F. J. Manjón, *J. Appl. Phys.*, 2014, 115, 043510.

24. R. C. Dai, L. B. Luo, Z. M. Zhang and Z. J. Ding, *Mater. Res. Bull.*, 2011, 46, 350-354.

25. M. R. Joya, J. Barba-Ortega and P. S. Pizani, *J. Appl. Phys.*, 2013, 113, 013512.

Figure captions

Fig. 1 SEM images of $YBO_3:Eu^{3+}$ sample; (a) as-prepared powder, (b) heat-treated at 1537 K.

Fig. 2 X-ray diffraction pattern of $YBO_3:Eu^{3+}$ sample.

Fig. 3 Excitation and phonon side band (PSB) spectra of $YBO_3:Eu^{3+}$ sample at ambient condition.

Fig. 4 PL spectra with Lorentz fitting of $YBO_3:Eu^{3+}$ sample at ambient condition.

Fig. 5 Raman scattering of $YBO_3:Eu^{3+}$ at temperature range of 298-1323 K (excited by 785 nm laser under 1323 K and 514.5 nm laser at 1323 K , respectively).

Fig. 6 PL spectra of $YBO_3:Eu^{3+}$ under 514.5 nm excitation during heating and cooling process.

Fig. 7 Temperature dependence decay curves of Eu^{3+} emission detected at 593 nm for $YBO_3:Eu^{3+}$ sample.

Fig. 8 Normalized total emission intensity of $^5D_0 \rightarrow {}^7F_{0,1,2,3}$ as a function of temperature. The dots are experimental data and the solid lines are fitting functions. The insert is population of $^7F_{0,1,2,3}$ levels as a function of temperature.

Fig. 9 PL spectra of $YBO_3:Eu^{3+}$ under 488 nm excitation during compression.

Fig. 10 Raman scattering of $YBO_3:Eu^{3+}$ under 488 nm excitation during compression and decompression.

Table 1. Energy levels and deviations of Eu^{3+} in $YBO_3:Eu^{3+}$ (units, cm^{-1})

$^7F_0$	$^7F_1$	$^7F_2$	$^7F_3$	$^5D_0$	$^5D_1$	$^5D_2$
0.0	280.8	814.0	1798.9	17218.4	19025.9	21533.2
	317.1	836.0	1812.0			21431.6
	330.6	867.3	1857.8			
	353.8	1247.0	1872.6			
	365.0	1285.7	1898.9			
	370.7		1950.7			
			2004.3			

Table 2. Raman active modes at ambient pressure with their pressure coefficients, as well as Grüneisen parameter γ and molar heat capacity for each mode

ω (cm^{-1})	dω/dp ($cm^{-1}\cdot GPa^{-1}$)	γ	*Ci* ($J\cdot mol^{-1}\cdot K^{-1}$)
209.9	1.56	1.05	7.65
264.5	1.89	1.01	7.28
301.2	1.99	0.93	7.01
363.2	1.68	0.65	6.50
382.5	3.23	1.19	6.33
416.7	1.92	0.65	6.02
436.7	2.77	0.89	5.84
513.8	3.1	0.85	5.13
618.7	2.64	0.60	4.18
838.5	3.98	0.67	2.50
1005	5.35	0.75	1.58
1038	5.98	0.81	1.44

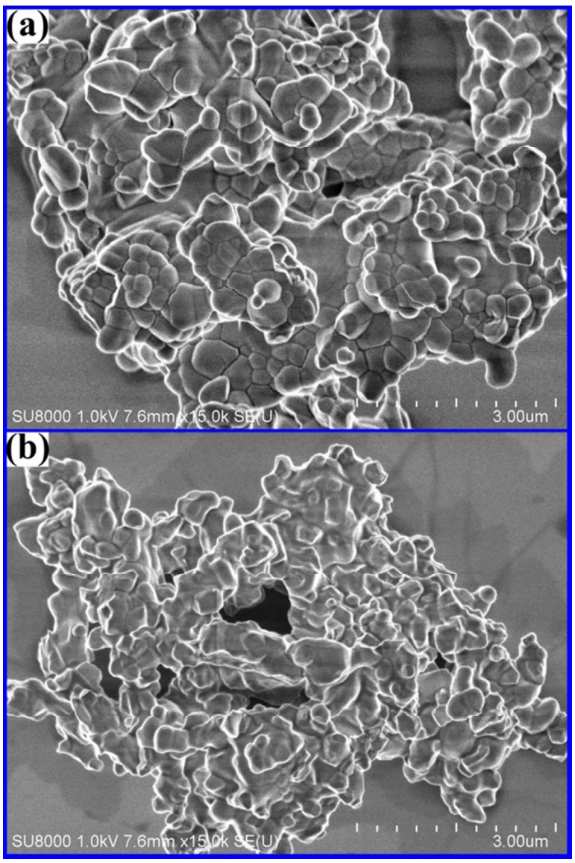

Fig. 1

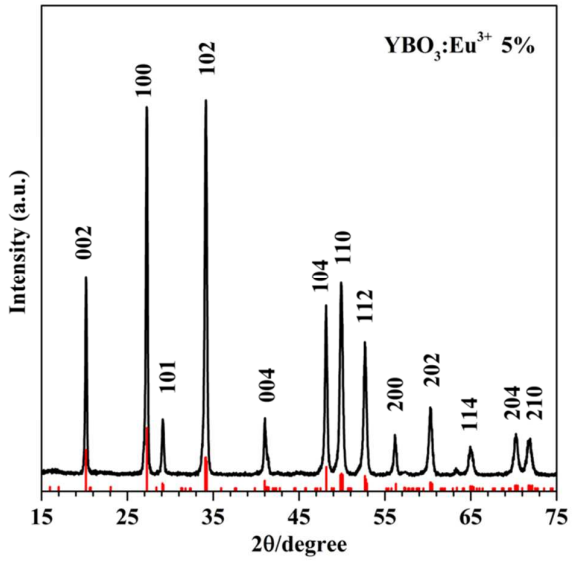

Fig. 2

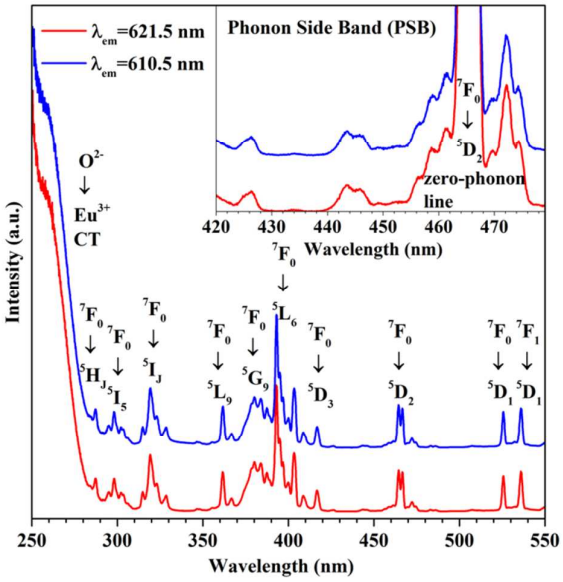

Fig. 3

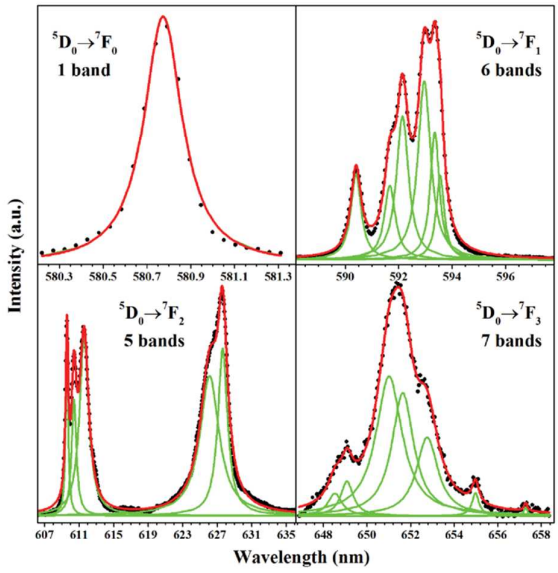

Fig. 4

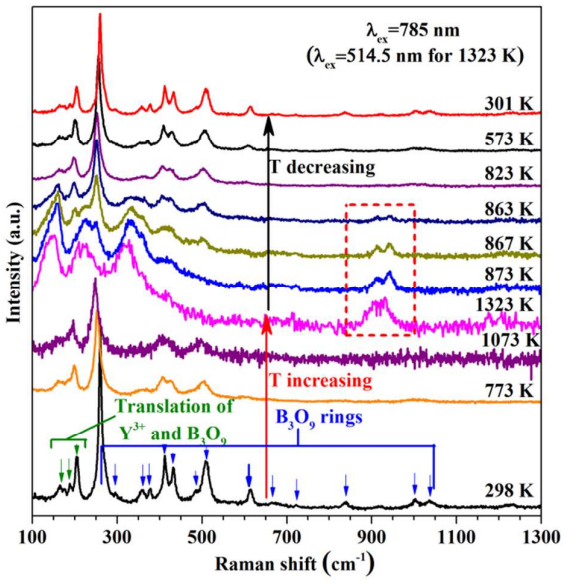

Fig. 5

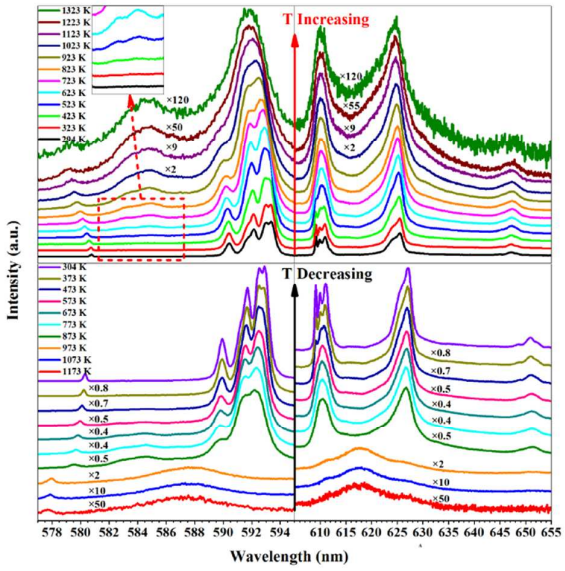

Fig. 6

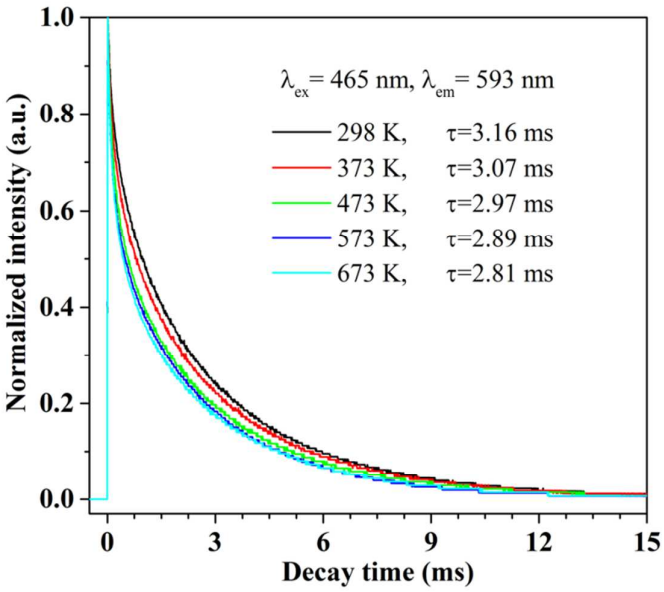

Fig. 7

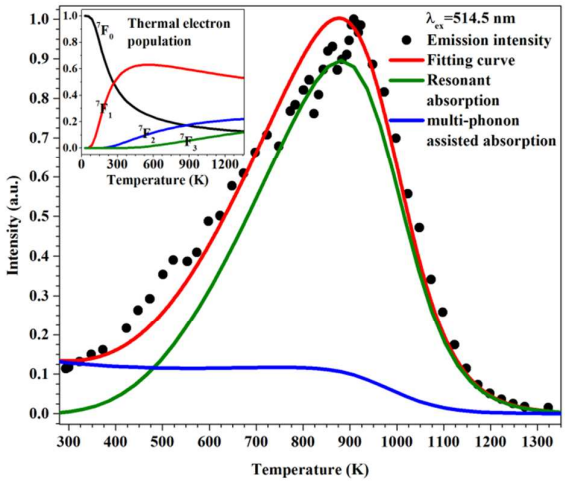

Fig. 8

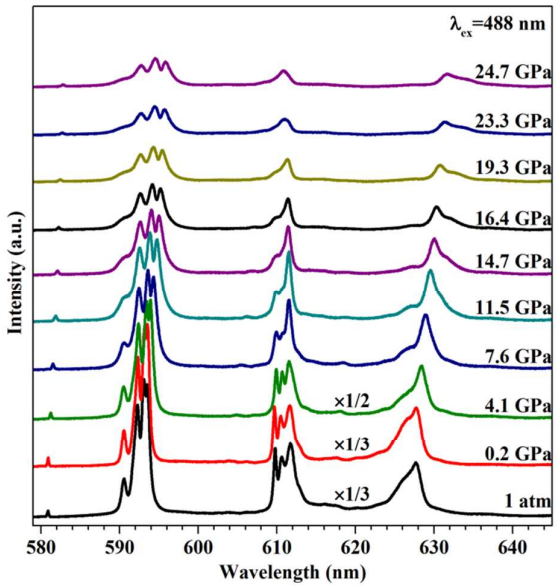

Fig. 9

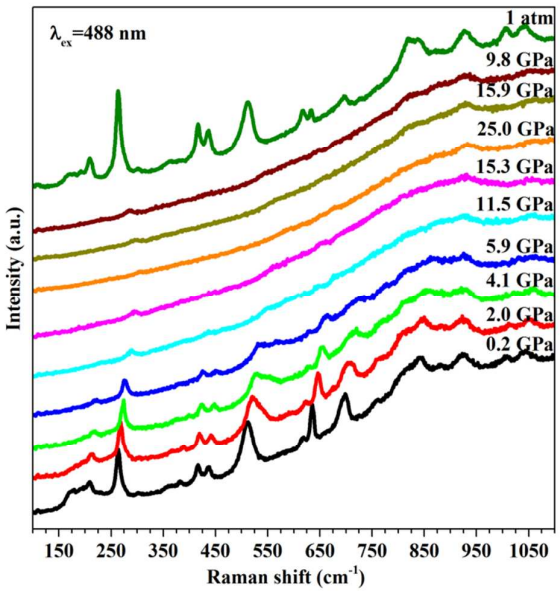

Fig. 10

The effect of temperature and pressure on structure of YBO_3:Eu was characterized by Raman scattering and on optical properties was analyzed by luminescent dynamic method.

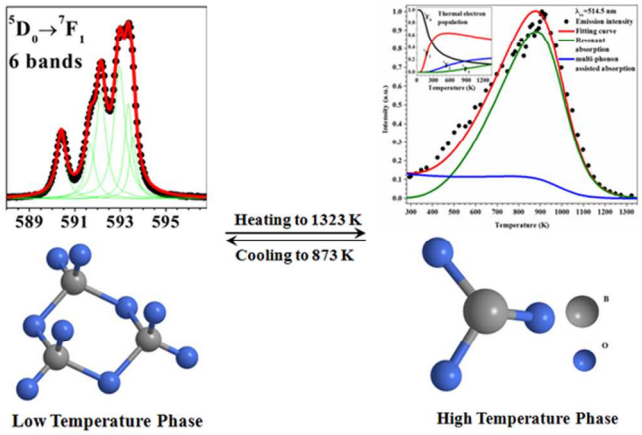

Graphical Abstract
79x39mm (300 x 300 DPI)